Supporting Information for

Oxygen-Tolerant Electroproduction of C$_2$ Products from Simulated Flue Gas

Yi Xu,‡ Jonathan P. Edwards,‡ Junjie Zhong, Colin P. O'Brien, Christine M. Gabardo, Christopher McCallum, Jun Li, Cao-Thang Dinh, Edward H. Sargent and David Sinton*
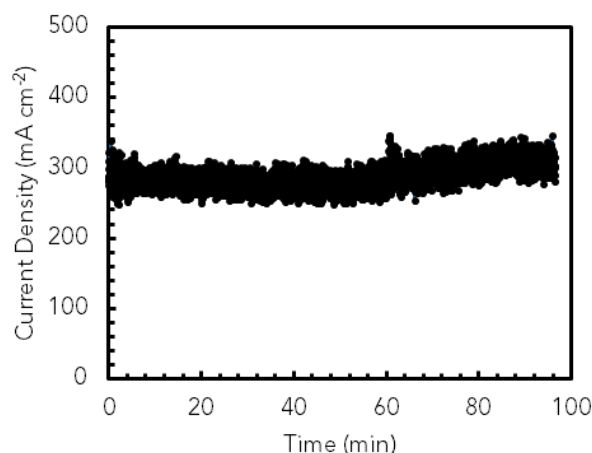
Fig S1. Current characteristics in the stability test of bare Cu catalyst at -3.00 V cell voltage and 10 bar.
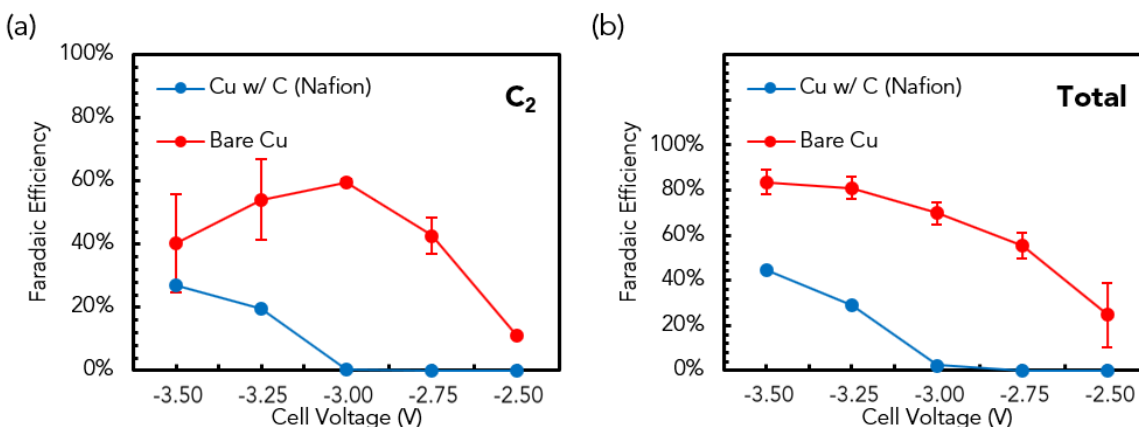
Fig S2. Effect of Nafion with carbon nanoparticles support layer ionomer on the performance of pressurized (10 bar) CO$_2$RR with 15% CO$_2$ (v/v) and 4% O$_2$ (v/v) feedstocks and 1M KOH electrolyte, comparing with bare Cu sample. (a) The FE towards C$_2$ products. (b) The total FE of both HER and CO$_2$RR products.
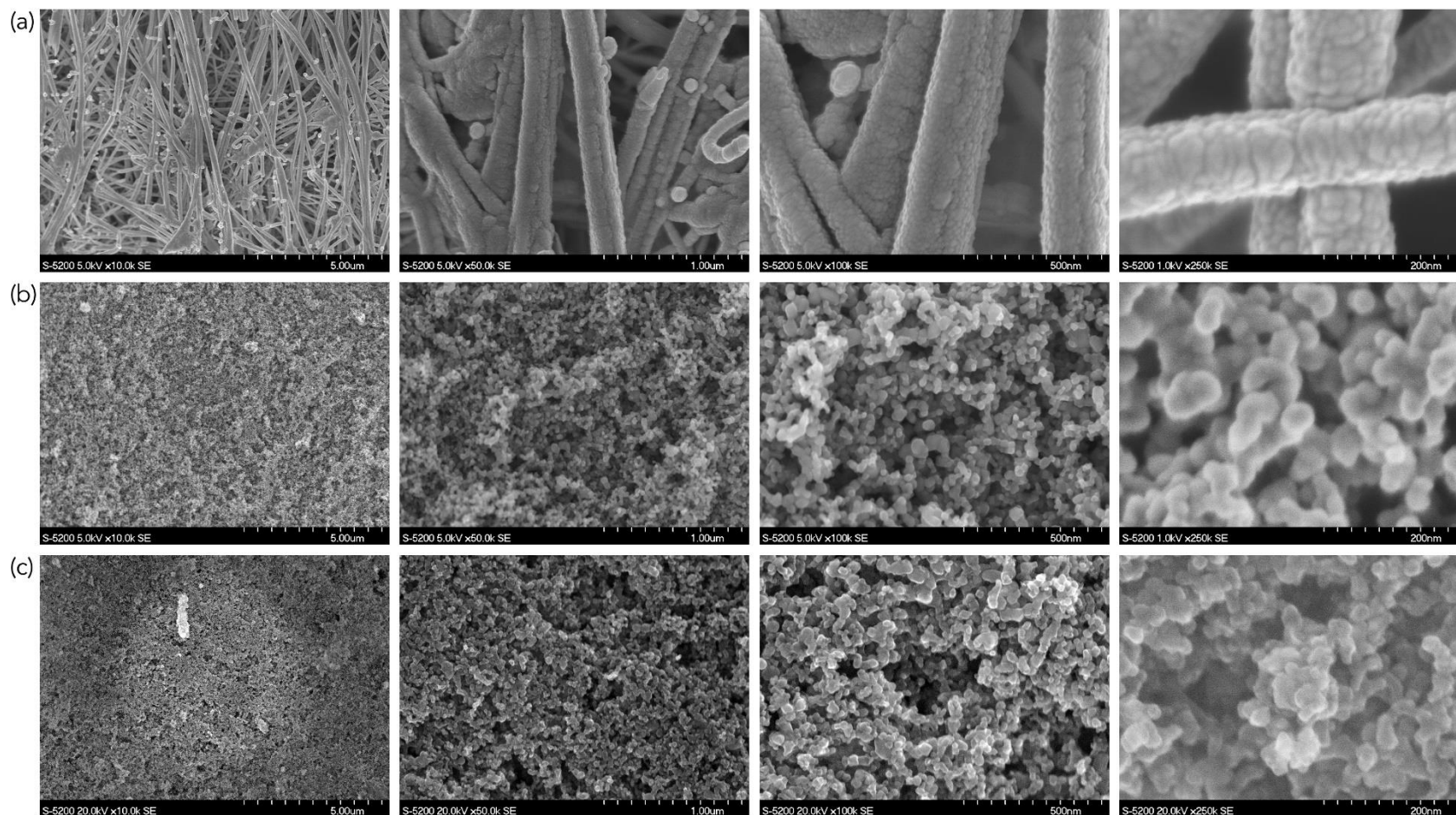
Fig S3. SEM images of the GDE with the scale bar of 5 μm, 1 μm, 500nm and 200nm from left to right. (a) 300 nm Cu cathode catalyst sputtered on PTFE fiber GDE. (b) Cu-PTFE GDE coated with *Hydrophilic-1* ionomer/TiO$_2$ support particles before prolonged operation. (c) Cu-PTFE GDE coated with *Hydrophilic-1* ionomer/TiO$_2$ support particles after prolonged operation.
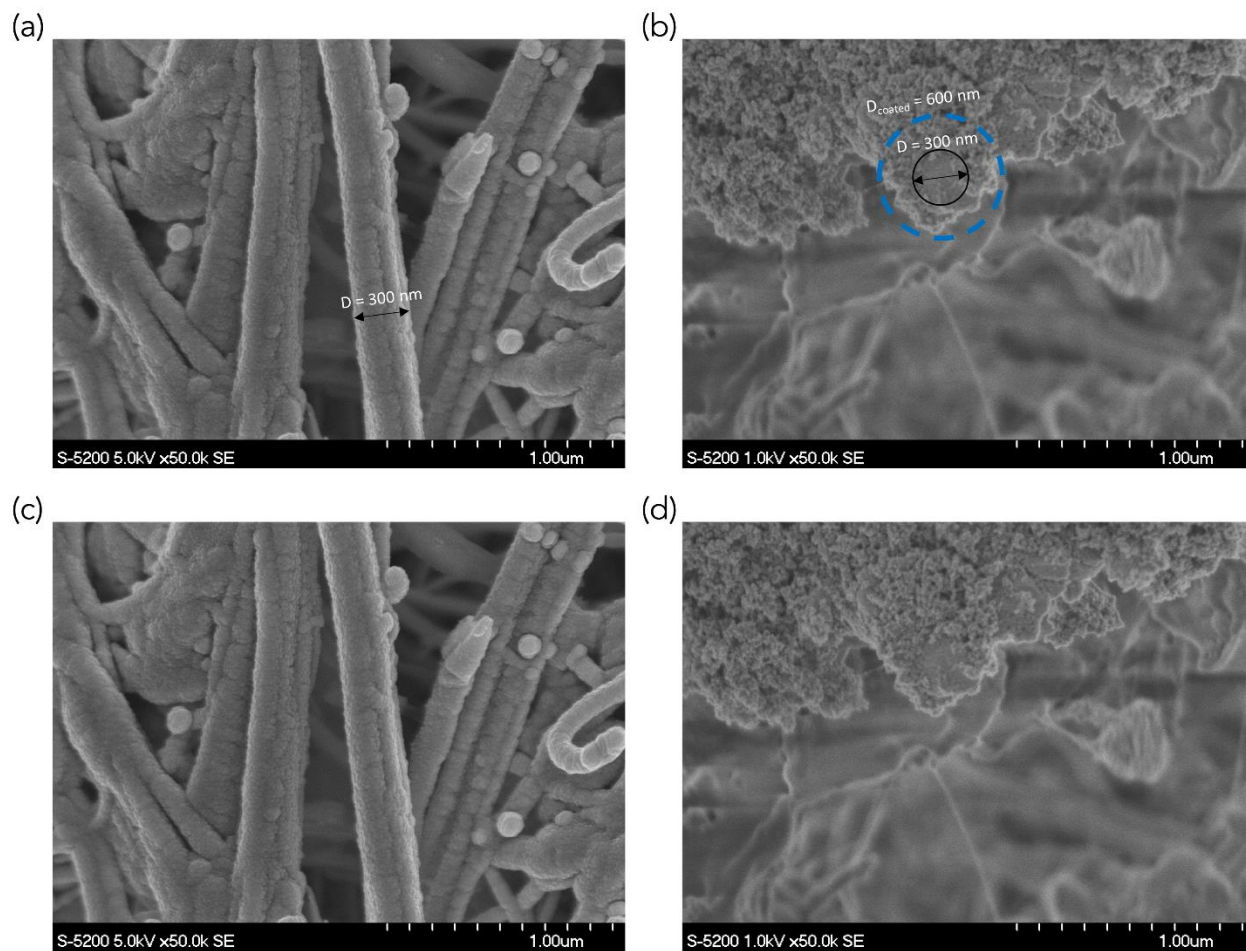
Fig S4. SEM images showing ionomer coverage on Cu catalyst. (a, c) Cu-PTFE GDE with and without labeling, respectively. (b, d) Cross-sectional SEM image of Cu-PTFE GDE coated with *Hydrophilic-1* ionomer/TiO$_2$ support particles with and without labeling, respectively.
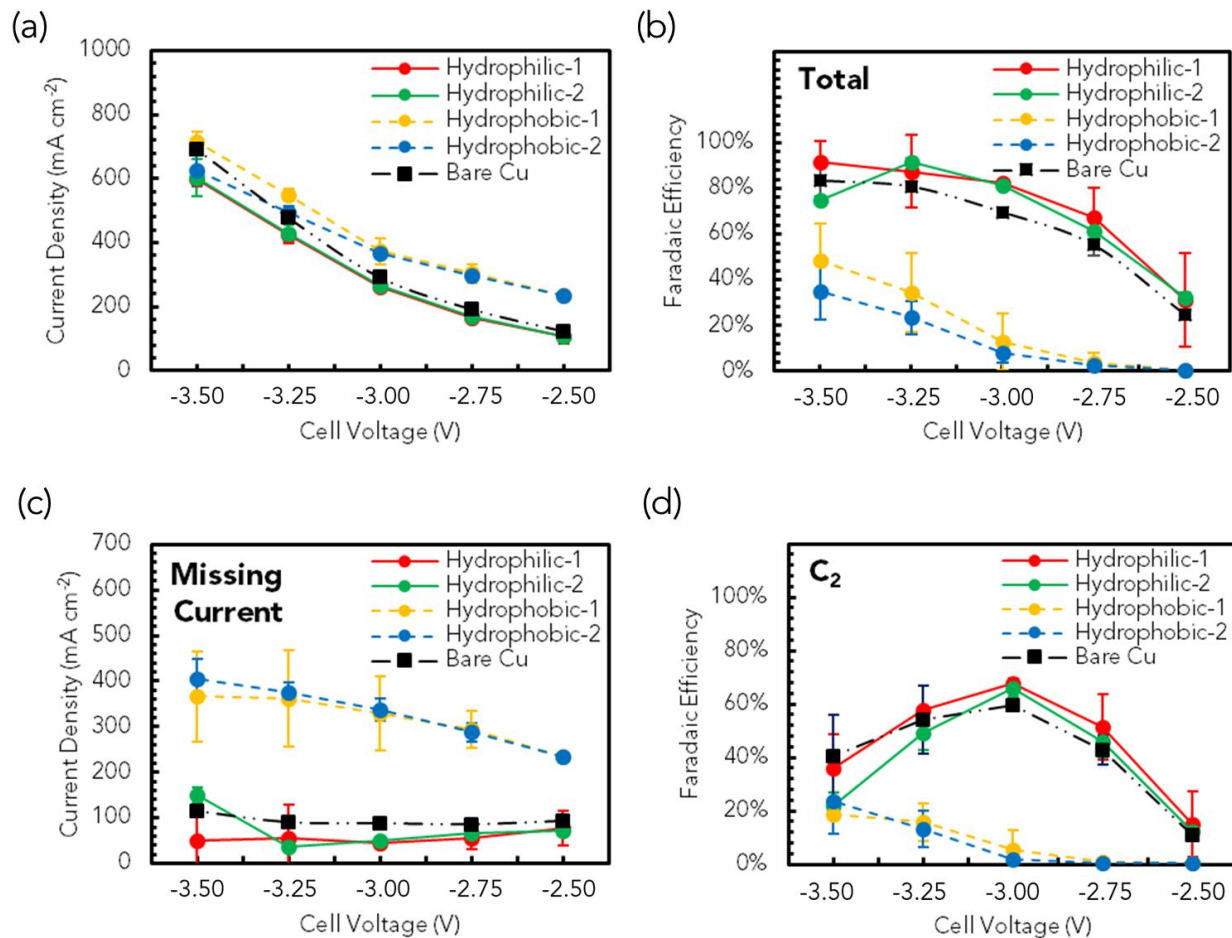
Fig S5. Effect of bare Cu and support layer ionomer on the performance of pressurized (10 bar) CO_2RR with 15% CO2 (v/v) and 4% O2 (v/v) feedstocks, 1M KOH electrolyte, and TiO_2 support particles. (a) Current-voltage characteristics with different ionomer coatings on Cu-PTFE GDE. (b) The total FE of both HER and CO2RR products. (c) Missing current density for the different ionomers calculated using the complement of the total FE. (d) The FE toward C_2 products for different ionomers.

Influence of hydrophobic and hydrophilic layers on oxygen transport when using non-ionomer coatings

To demonstrate that the slowing of oxygen transportation is due to the hydrophilicity of the support layer - independent of the cation or anion exchange effects - we coated the non-ionomer polymer polydimethylsiloxane (PDMS) on top of the catalyst layer. PDMS inherently generates hydrophobic nanoporous structures,[1] but these structures can become hydrophilic from plasma treatment.[2]

To prepare the samples, we first diluted the PDMS in the hexane solution with a 1:4 mass ratio. Then, we coated 1.2 mg cm^{-2} of PDMS on Ag-sputtered PTFE GDE. After coating, the PDMS Ag-PTFE GDE was baked in the oven at 60 $^{\circ}$C for five hours. Half of the samples were then kept for the hydrophobic experiments, while the other half were treated in a PDC – 32G Harrick plasma cleaner for one hour.
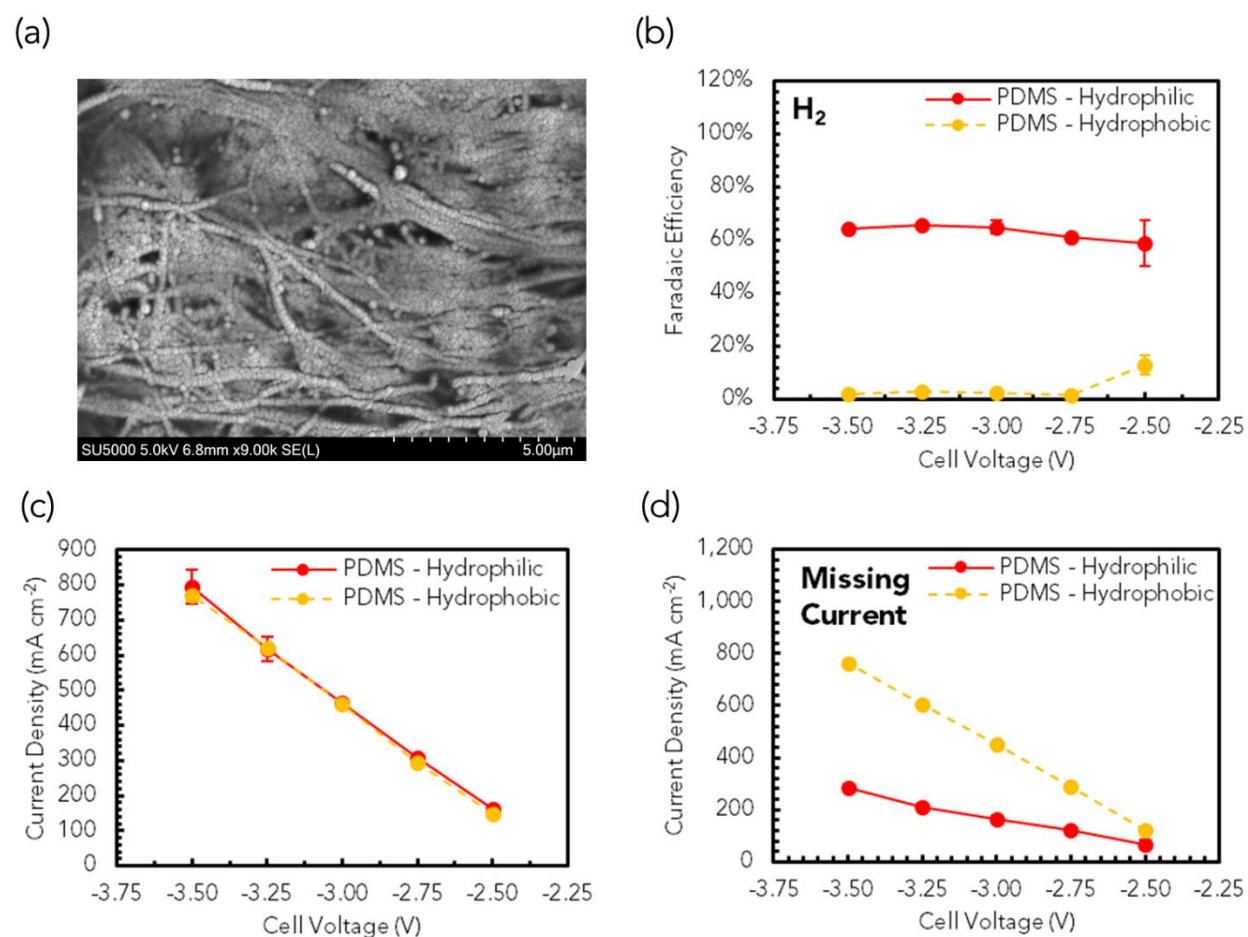
Fig S6. Influence of binder hydrophilicity for non-ionomer binders coated on Ag-PTFE GDE performed with air, 1 M KOH electrolyte, 1 bar, and TiO$_2$ support particles. (a) SEM image of PDMS coated Ag-PTFE GDE. (b) The FE toward H$_2$ for the hydrophilic and hydrophobic PDMS coatings on Ag-PTFE GDE. (c) Current-voltage characteristics with hydrophilic and hydrophobic PDMS coatings on Ag-PTFE GDE. (d) Missing current density for hydrophilic and hydrophobic PDMS coatings on Ag-PTFE GDE calculated using the complement of the H$_2$ FE.

Influence of ionomer hydrophobicity on CO₂ mass transport

Silver (Ag) was selected as the CO_2RR catalyst because it is known to produce only three major products (carbon monoxide, formate, and acetate) from CO_2RR thereby simplifying the assessment of limiting current density. TiO_2 nanoparticles were sprayed with the ionomer for consistency with previous experiments in this work.
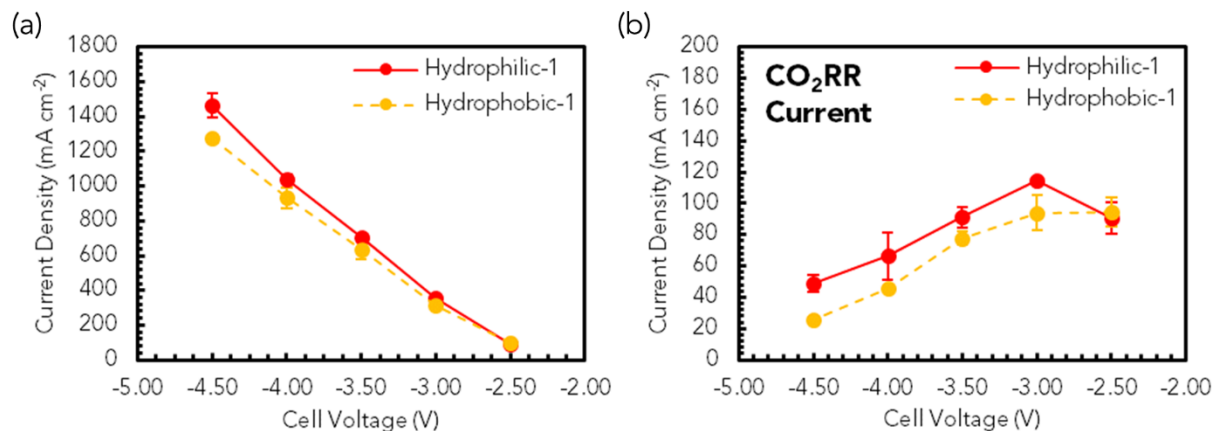
Fig S7. CO_2 transport comparison for hydrophilic and hydrophobic ionomer coatings on an Ag-PTFE GDE performed with 100% CO_2, 1 atm, 1 M KOH electrolyte, and TiO_2 support particles. (a) The total current as a function of the cell voltage. (b) The partial current towards CO_2RR at different cell voltages.
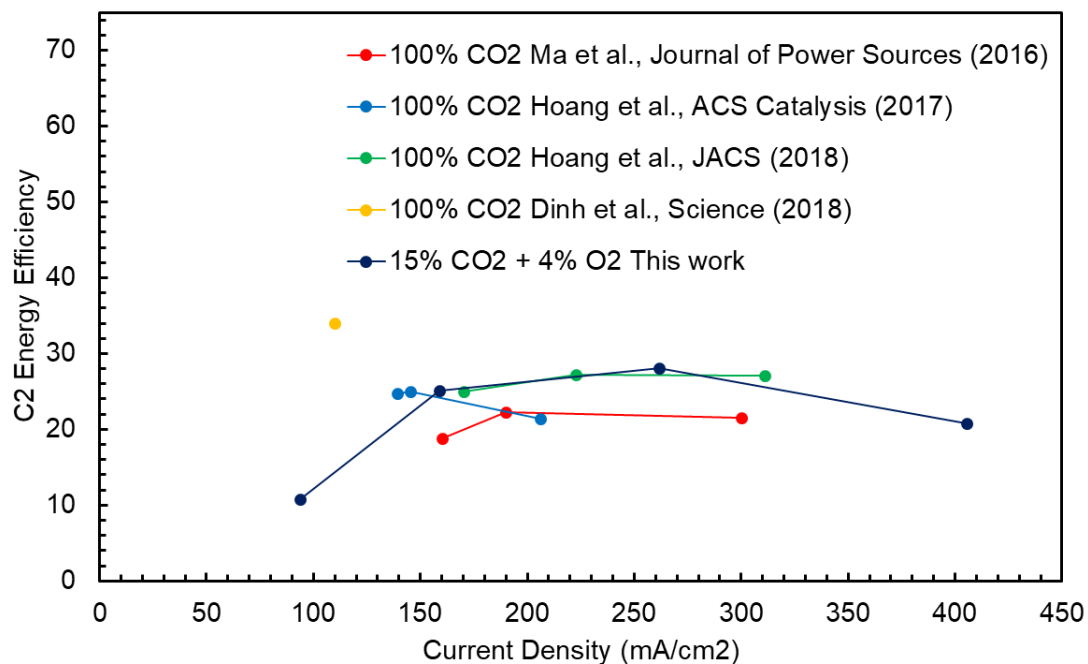
Fig S8. Comparison with the previous CO_2RR to C_2 product data reports at high EE. The references are from Ma et al., Journal of Power Sources;[3] Hoang et al., ACS Catalysis;[4] Hoang et al., JACS[5] and Dinh et al., Science.[6]

Diffusivity Simulation of Carbon Dioxide (CO₂) and Oxygen (O₂) in Nanoporous Media

For gas molecules diffusing through a microporous membrane (here Nafion 117, pore size characterized at 2-nm)[7], the pore size is comparable with gas molecular mean free path. The overall gas diffusivity (D_v) described through Bosanquet relation[8]:

$$D_v = \left(D_b^{-1} + D_{Kn}^{-1}\right)^{-1} \tag{1}$$

Where D_b is the gas bulk diffusivity, and D_{Kn} is the gas Knudsen diffusivity. The value of D_b and D_{Kn} can be further expressed as a function of molecular mean free (λ) path and pore diameter (d_p), and D_v becomes:

$$D_v = \left(\frac{3}{u\lambda} + \frac{3}{ud_p}\right)^{-1} \tag{2}$$

Where u is the mean velocity of gas molecules. From the gas kinetic theory:

$$\lambda = \frac{k_B T}{\sqrt{2}\pi d_m{}^2 P} \tag{3}$$

$$u = \sqrt{\frac{8RT}{\pi M}} \tag{4}$$

Where k_B is the Boltzmann constant, T is gas temperature (here 398 K), d_m is the molecular kinetic diameter (3.3 Å for CO₂ and 3.46 Å for O₂)[9], P is gas pressure (here for CO₂ is $1.5 \times 10^5\ Pa$, and for O₂ is $4 \times 10^4\ Pa$), R is the gas constant and M is the molecular mass ($44 \times 10^{-3}\ kg/mol$ for CO₂ and $36 \times 10^{-3}\ kg/mol$ for O₂). From equations (2)-(4), the overall gas phase diffusivity for CO₂ is $2.44 \times 10^{-7}\ m^2/s$, and for O₂ is $2.93 \times 10^{-7}\ m^2/s$.

For dissolved phase diffusion in 1 M KOH solution reaching steady state, the CO₂ and O₂ solubility in the liquid electrolyte solution is low, and the system can be thus treated as a weak solution for dissolved gas. The dissolved gas diffusivity in KOH solution (D_l) herein can be calculated through the semi-empirical Wilke-Chang correlation[10]:

$$D_l = 1.173 \times 10^{-16} \frac{(\varphi M_s)^{0.5} T}{\mu_s V_g{}^{0.6}} \tag{5}$$

Where φ is an association parameter (here for 1 M KOH aqueous solution taking the value for water as 2.6), M_s is the molecular mass of the solution ($\sim 18\ kg/kmol$), μ_s is the viscosity of solution (here $\sim 1.28 \times 10^{-4}\ Pa.s$)[11], V_g is the molar volume at normal boiling point (for CO₂ is $0.034\ m^3/kmol$ and for O₂ is $0.0256\ m^3/kmol$). As a result, the dissolved phase diffusivity in KOH solution for CO₂ is $1.51 \times 10^{-9}\ m^2/s$, and for O₂ is $1.80 \times 10^{-9}\ m^2/s$.

CO₂ and O₂ Mass Transfer Rate Simulation in the Hydrophobic and Hydrophilic Nanopores

1. CO₂ and O₂ mass transfer rate simulation in the hydrophobic nanopores
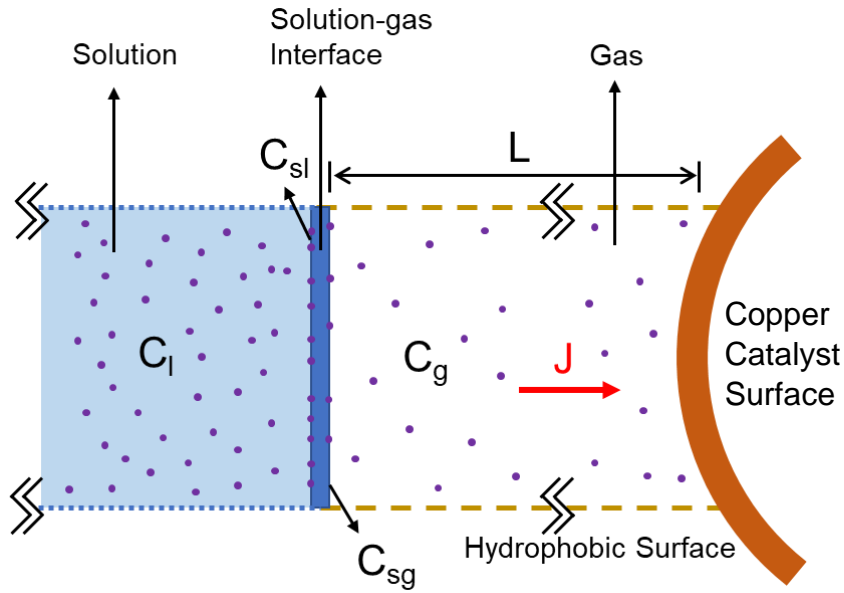
Fig S9. Schematic of CO₂ and O₂ concentration distribution around the solution-gas interface in hydrophobic nanopores.

In the mass transfer rate simulation, O₂ will be demonstrated first. As shown in Figure S5, when performing electroreduction with hydrophobic nanoporous media, the dissolved O₂ molecules will be degassed from the solution-gas interface, and then gas-phase O₂ would fast travel through the hydrophobic nanoporous. The mass flux at unit area (J) governed by the solution-gas interface can be expressed as[12]:

$$J = K_g(C_{sg} - C_g) = K_l(C_l - C_{sl}) \tag{6}$$

Where C_{sg} is the O₂ concentration on the gas side of the solution-gas interface, C_{sl} is the O₂ concentration on the liquid side of the solution-gas interface, C_g is the gas concentration in gas mixture confined in the hydrophobic nanopore, C_l is the gas concentration in the KOH liquid solution (= 0.347 mol m⁻³ at 4% O₂ concentration in 10 bar mixture gas for our experiments with the Sechenov equation to account for reduced gas solubility in salt-containing solutions),[13] K_g and K_l are the exit coefficient at the gas and liquid side of solution-gas interface, respectively. The relation between C_{sg} and C_{sl} is described by the Henry volatility constant and degasification coefficient k_d:

$$C_{sg} = K_H k_d C_{sl} \tag{7}$$

Where, and K_H is the volatile constant (for O₂ in water is 31.25), k_d the degasification ratio respects to time, which is the measured experimentally to be 1.001×10⁻⁴.[14]

The exit coefficients (K_g and K_l) at a regularly renewed interface (here gas molecules are released from the solution through the interface and quickly go to the copper for electroreduction) are[15]:

$$K_g = 2\sqrt{\frac{D_g}{\pi t}} \tag{8}$$

$$K_l = 2\sqrt{\frac{D_l}{\pi t}} \tag{9}$$

Where D_g is the O_2 diffusivity in the gas mixture (2.93×10^{-7} m^2 s^{-1}), D_l is the dissolved O_2 diffusivity in KOH solution (1.80×10^{-9} m^2 s^{-1}), and t is the exposure time of the interface. In our system, the exposure time can be characterized by the mass flux as:

$$t = \frac{C_g L}{J} \tag{10}$$

and L is the average distance between O_2 molecules:

$$L = \sqrt[3]{\frac{k_B T}{P}} \tag{11}$$

Where T is the experimental system temperature (293 K), and P is the gas pressure (1 MPa).

Combing equation (6) to (10), the expression of the mass flux can be further expressed as:

$$J = \frac{K_H k_d C_l - C_g}{\left(1/(2\sqrt{\frac{D_g}{\pi t}}) + K_H k_d/(2\sqrt{\frac{D_l}{\pi t}})\right)} \tag{12}$$

A one-dimensional model of the O_2 gas concentration within the catalyst layer necessitates the solution of the following equation at steady-state conditions:

$$D_g \frac{\delta^2 [C_g]}{\delta x^2} - R_g = 0 \tag{13}$$

R_g is the rate of O_2 gas consumption. Assuming a uniform reaction rate throughout the catalyst layer yields the following equation:

$$R_g = \frac{J}{L_{nanopore}} \tag{14}$$

Here $L_{nanopore}$ denotes the mean distance that gas molecule has to travel from the out surface of ionomer to the surface of the catalyst. (300 nm average diameter for the catalyst samples used in these experiments, 600 nm average diameter for the ionomer coated samples. The mean distance $= (600 + 300)/2 \times \pi/2 = 707$ nm.)

The solution to the above equation is of the following form:

$$[O_2] = \frac{J}{2L_{nanopore}D_g}x^2 + C_1x + C_2 \tag{15}$$

Boundary conditions are required to solve for the necessary constants. The first boundary condition is that the gas concentration at the gas-liquid interface (e.g., at x = 0) is equal to the maximum solubility of O_2 in the electrolyte denoted by C_g. From this condition, the following relation is obtained:

$$C_2 = C_g \tag{16}$$

The secondary boundary condition for this model assumes that there is no flux of gas molecule into the bulk electrolyte. From this information, the following relation is obtained:

$$C_1 = \frac{J}{D_g} \tag{17}$$

Re-writing the solution with the known constants yields:

$$[O_2] = \frac{J}{L_{nanopore}D_g}\left(\frac{1}{2}x^2 - L_{nanopore}x\right) + C_g \tag{18}$$

Assuming that the reaction rate is purely determined by mass-transport limitations (as opposed to electrochemical limitations) we assume that the O_2 gas concentration at the furthest edge of the catalyst layer (e.g., x = $L_{nanopore}$) is equal to zero. Substituting this condition into the above solution and rearranging allows for an estimation of the diffusion coefficient for O_2 in the system:

$$J = \frac{D_{O2}L_{nanopore}}{2C_o} \tag{19}$$

Combing equation (19) to (12), the O_2 mass flux of traveling through the hydrophobic ionomer nanopores networks can be calculated as 7.66×10^{-3} mol m^{-2} s^{-1}.

Using equation (6) to (19) and the simulated CO_2 diffusivity of gas and dissolved phase, CO_2 mass flux of traveling through the hydrophobic ionomer nanoporous networks can be calculated, which is 2.65×10^{-2} mol m^{-2} s^{-1}.

2. CO_2 and O_2 mass transfer rate simulation in the hydrophilic nanopores
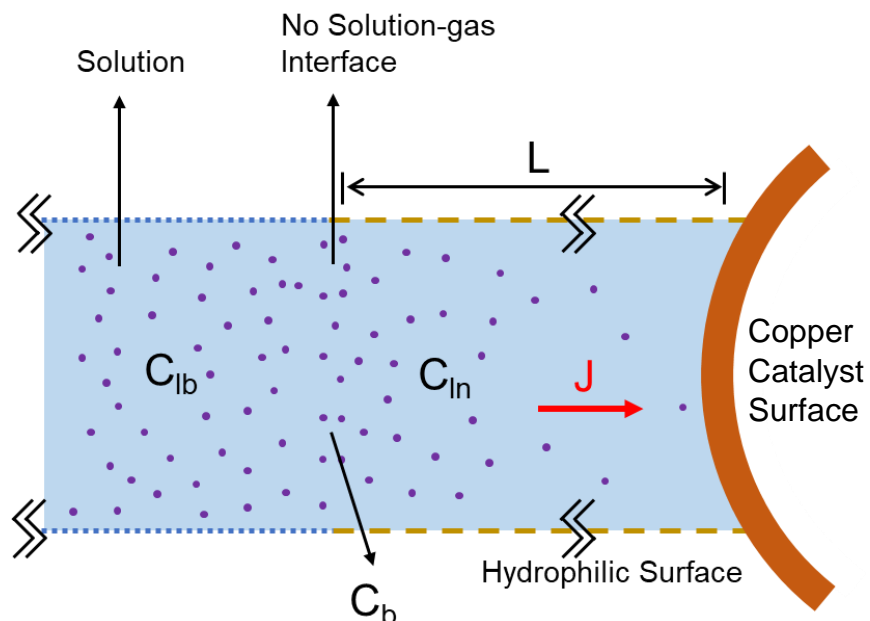
Fig S10. Schematic of CO_2 and O_2 concentration distribution in hydrophilic nanopores.

In the CO_2 and O_2 mass transfer rate simulation in the Hydrophilic Nanopores, there is no solution-gas interface. The bulk phase saturated dissolved CO_2 and O_2 can directly diffuse into the hydrophilic nanopores. Therefore, the boundary condition of dissolved CO_2 and O_2 is the saturated concentration C_b in bulk phase electrolyte, which are 3.40×10^1 mol/m^3 and 3.47×10^{-1} mol/m^3, respectively. Using the equation (19) and simulated dissolved phase CO_2 and O_2 hydrophilic nanoporous diffusivities, the mass flux towards to the catalyst surface can be calculated (3.63×10^{-2} mol m^{-2} s^{-1} for CO_2, 4.41×10^{-4} mol m^{-2} s^{-1} for O_2).

Experimental O$_2$ Mass Transfer Rate Calculation of in Nanoporous Media

The rate of O$_2$ consumption is solely due to the electrochemical reaction. The following equation is used to calculate the experimental O$_2$ mass flux:

$$J = \frac{j_{ORR}}{zF}$$

(20)

Here j$_{ORR}$ denotes the maximum current density towards O$_2$ reduction, z denotes the number of electrons transferred per molecule of O$_2$ reduced (4 from the reaction stoichiometry), F is Faraday's constant (valued at 96485 C/mol e$^-$). Since the missing currents in the electrochemical reaction are used to quantify the current towards O$_2$ reduction, the missing current results (shown in fig. 3f) are substituted in the equation above (45 mA/cm^2 for Sustainion hydrophilic ionomer nanopores, 380 mA/cm^2 for Nafion hydrophobic ionomer nanopores).

Table 1. O$_2$ mass flux comparison between simulated and experimental results.

	Simulated mass flux results (mol m^{-2} s^{-1})	Experimental mass flux results (mol m^{-2} s^{-1})
O$_2$ in hydrophobic nanopores	7.66×10^{-3}	9.85×10^{-3}
O$_2$ in hydrophilic nanopores	0.44×10^{-3}	1.14×10^{-3}

From the O$_2$ mass flux comparison above, the simulated hydrophobic nanopores result is agreed with the experiment very well. The O$_2$ in hydrophilic nanopores shows a smaller simulated mass flux than experiments. The major reason is that the relatively small missing current in hydrophilic nanopores is very sensitive to the uncertainty of the gas and liquid sample measurement. The most significant finding in this comparison is that the simulated and experimental results both proved the hydrophilic nonporous networks could efficiently reduce the O$_2$ mass flux towards to the catalyst surface more than eight times than the hydrophobic one.

Table 2. Effect of support layer ionomer on the performance of pressurized (10 bar) CO_2RR with 15% CO_2 (v/v) and 4% O_2 (v/v) feedstocks, 1M KOH electrolyte, and TiO_2 support particles.

	Full cell Potential (V)	Current Density (mA cm^{-2})	Faradaic Efficiency (%)						
			H$_2$	CO	CH$_4$	C$_2$H$_4$	Format e Acid	Acetate Acid	Ethanol
Cu-PTFE GDE coated with *Hydrophilic-1* ionomer /TiO$_2$ support particles	-2.50	109.9	7.1%	4.7%	0.1%	11.1%	4.4%	1.4%	2.5%
	-2.75	164.5	8.3%	3.6%	0.5%	36.9%	3.4%	2.5%	12.0%
	-3.00	261.4	9.0%	3.2%	1.2%	48.2%	1.5%	3.6%	16.0%
	-3.25	426.2	22.1%	2.1%	4.7%	30.8%	0.9%	6.0%	21.1%
	-3.50	598.2	39.6%	4.2%	11.4%	17.9%	0.6%	5.3%	12.8%
Cu-PTFE GDE coated with *Hydrophilic-2* ionomer /TiO$_2$ support particles	-2.50	107.9	8.5%	9.7%	0.2%	11.7%	3.6%	1.3%	0.0%
	-2.75	171.6	5.2%	4.8%	1.1%	33.3%	4.1%	2.9%	10.0%
	-3.00	266.5	7.3%	2.0%	3.8%	44.3%	2.5%	4.4%	17.3%
	-3.25	430.5	25.8%	0.0%	15.4%	26.4%	1.3%	5.5%	17.4%
	-3.50	602.9	31.7%	0.0%	20.5%	9.3%	0.8%	4.2%	8.6%
Cu-PTFE GDE coated with *Hydrophobic-1* ionomer /TiO$_2$ support particles	-2.50	234.4	0.1%	0.0%	0.0%	0.3%	0.0%	0.0%	0.0%
	-2.75	304.4	0.8%	1.8%	0.1%	0.6%	0.1%	0.2%	0.0%
	-3.00	373.6	2.5%	4.5%	0.0%	4.3%	0.2%	0.1%	1.2%
	-3.25	549.4	12.8%	4.7%	0.7%	10.1%	0.6%	1.3%	4.4%
	-3.50	716.6	24.5%	3.2%	1.6%	11.1%	0.5%	2.0%	5.8%
Cu-PTFE GDE coated with *Hydrophobic-2* ionomer /TiO$_2$ support particles	-2.50	235.9	0.1%	0.0%	0.0%	0.1%	0.0%	0.3%	0.0%
	-2.75	295.9	0.2%	1.8%	0.0%	0.2%	0.2%	0.4%	0.0%
	-3.00	366.6	0.6%	4.9%	0.0%	1.4%	0.6%	0.2%	0.0%
	-3.25	493.4	1.6%	7.7%	0.1%	8.1%	1.1%	0.9%	4.1%
	-3.50	625.6	3.2%	6.7%	0.5%	16.2%	0.9%	1.4%	6.1%

Calculation of Full Cell Faradaic Efficiency (FE) and Energetic Efficiency (EE)

The FE of each gas product is calculated by the following equation:

$$FE_{gas} = x_i \times v \times \frac{z_i F P_0}{RT} \times \frac{1}{I_{total}} \times 100\% \tag{21}$$

Where x_i is the volume fraction of gas product i, v is the gas flow rate at the outlet in standard cubic centimeters per minute, z_i is the number of electrons required to produce one molecule of product i, F is the Faraday Constant, P_0 is 101325 Pa, R is the ideal gas constant, T is the temperature, and I_{total} is the total current.

The FE of each liquid product is calculated by the following equation:

$$FE_{liquids} = n_i \times \frac{z_i F}{Q} \times 100\% \tag{22}$$

Where n_i is the number of moles of product i, and Q is the charge passed while the liquid products are being collected.

The full cell voltage efficiency is calculated as for each product by the following equation:

$$VE_{full\ cell} = \frac{E^o_{cell}}{E_{cell}} \times 100\% \tag{23}$$

$$E^o_{cell} = \frac{\Delta G^o}{-zF} \tag{24}$$

Where, E^o_{cell} is the thermodynamic cell potential for each product, ΔG^o is the change in Gibbs free energy for the reaction, and E_{cell} is the applied cell voltage (non-iR compensated).

The full cell energy efficiency is calculated by the following equation:

$$EE = \sum_{i}^{n} VE_i \times FE_i \tag{25}$$

Energy Requirement of the Gas Pressurization

To estimate the energy requirements for simulated flue gas (15% CO_2 + 4% O_2 balancing with nitrogen) pressurization to 10 bar from 1 bar, it is assumed that a three-stage compressor is used. It should be noted that pressurization process could be performed more efficiently if a more than the three-stage compressor is applied.[16] To minimize the total work required to pressurize the flue gas, an approximate equivalent enthalpy increment is employed at each compression stage. After each compression stage, the compressed gas is cooled back to the initial temperature in the intercoolers. The specific compressor work for each stage is given by:

$$w_{Compressor} = h_2 - h_1 \qquad\qquad (26)$$

Where h_2 and h_1 are the specific enthalpies of the fluid at the after and before compression, respectively.

Table 3. Thermodynamic conditions of ideal three-stage simulated flue gas compressor.[17]

	Initial Pressure (bar)	Final Pressure (bar)	Initial Enthalpy (kJ kg^{-1})	Final Enthalpy (kJ kg^{-1})	Entropy (kJ kg^{-1} K^{-1})	$w_{Compressor}$ (kJ kg^{-1})
Stage 1	1	2.2	350.03	421.31	6.0945	71.28
Stage 2	2.2	4.6	349.65	415.81	5.8790	66.16
Stage 3	4.6	10	348.90	418.87	5.6763	69.97
Total						207.41

Entering the compressor at 1 bar, 298 K, the simulated flue gas has specific enthalpy and entropy values of 350.03 kJ/kg and 6.0945 kJ/kg·K respectively. Utilizing the three-stage compressor, the ideal total work needs to compress the flue gas to 10 bar is 207.41 kJ kg^{-1} (0.2 GJ ton^{-1}). Considering the 90% mechanical efficiency the compressor and US$0.03 kWh^{-1} renewable electricity price,[18,19] the cost of the flue gas pressurization is US$1.9 ton^{-1}. Adding the compressor capital cost, ordinary maintenance cost and extraordinary maintenance cost, the total expense of 10 bar flue gas pressurization is approximately US$2.3 per ton.[20] Considering the 15% mole fraction concentration CO_2 in flue gas, the gas pressurization cost is ~$15 per ton CO_2 equivalent flue gas.

Energy Requirement of CO_2RR and Comparison with Gas Pressurization

The specific electrical energy to the CO_2RR depends on the number of electrons transferred per molecule of CO2 converted (z = 6 for CO_2 reduction to ethylene and ethanol, which are the majorities of our C_2 products),

$$w_{Electrical} = zFE \tag{6}$$

Where, Faraday's constant (F = 96485 C/mol e⁻), and the voltage applied (E) is the cell voltage of 3.00 V. As discussed in the manuscript at we achieve the peak FE_{C2} of 68% at 3.00V.

$$W_{Electrical} = \left(6 \ \frac{mol \ e^-}{mol \ CO_2}\right)\left(96485 \ \frac{C}{mol \ e^-}\right)(3.00 \ V)\left(\frac{1 \ mol \ CO_2}{44.01 \ g \ CO_2}\right) = 39462.17 \ \frac{J}{g} = 39.4 \ \frac{GJ}{ton}$$

Comparing with the energy requirement of the flue gas pressurization calculated previously (1.3 GJ per ton CO_2 equivalent to 10 bar pressure), the flue gas pressurization is only approximately 3% of the energy required to perform efficient CO_2RR to C_2 products.

Reference:

1   N. Bowden, A. Terfort, J. Carbeck and G. M. Whitesides, *Science (80-.).*, 1997, **276**, 233–235.

2   W. S. Liao, S. Cheunkar, H. H. Cao, H. R. Bednar, P. S. Weiss and A. M. Andrews, *Science (80-.).*, 2012, **337**, 1517–1521.

3   S. Ma, M. Sadakiyo, R. Luo, M. Heima, M. Yamauchi and P. J. A. Kenis, *J. Power Sources*, 2016, **301**, 219–228.

4   T. T. H. Hoang, S. Ma, J. I. Gold, P. J. A. Kenis and A. A. Gewirth, *ACS Catal.*, 2017, **7**, 3313–3321.

5   T. T. H. Hoang, S. Verma, S. Ma, T. T. Fister, J. Timoshenko, A. I. Frenkel, P. J. A. Kenis and A. A. Gewirth, *J. Am. Chem. Soc.*, 2018, **140**, 5791–5797.

6   C. T. Dinh, T. Burdyny, G. Kibria, A. Seifitokaldani, C. M. Gabardo, F. Pelayo García De Arquer, A. Kiani, J. P. Edwards, P. De Luna, O. S. Bushuyev, C. Zou, R. Quintero-Bermudez, Y. Pang, D. Sinton and E. H. Sargent, *Science (80-.).*, 2018, **360**, 783–787.

7   C. H. Chia, Z. Wu, C. H. Wu, R. H. Cheng and S. Ding, *J. Mater. Chem.*, 2012, **22**, 22440–22445.

8   D. Shou, J. Fan, M. Mei and F. Ding, *Microfluid. Nanofluidics*, 2014, **16**, 381–389.

9   N. W. Ockwig and T. M. Nenoff, *Chem. Rev.*, 2007, **107**, 4078–4110.

10   C. R. Wilke and P. Chang, *AIChE J.*, 1955, **1**, 264–270.

11   P. M. Sipos, G. Hefter and P. M. May, *J. Chem. Eng. Data*, 2000, **45**, 613–617.

12   P. . Liss, *Deep Sea Res. Oceanogr. Abstr.*, 1973, **20**, 221–238.

13   S. Weisenberger and A. Schumpe, *AIChE J.*, 1996, **42**, 298–300.

14   I. B. Butler,', M. A. A. Schoonen' and D. T. Rickard', *REMOVAL OF DISSOLVED OXYGEN FROM WATER: A COMPARISON OF FOUR COMMON TECHNIQUES*, 1994, vol. 41.

15   A. L. Downing and G. A. Truesdale, *J. Appl. Chem.*, 1955, **5**, 570–581.

16   M. J. Moran, H. N. Shapiro, D. D. Boettner and M. B. Bailey, *Fundamentals of Engineering Thermodynamics*, John Wiley & Sons Inc., Hoboken, NJ, 8th edn., 2014.

17   NIST, *NIST Stand. Ref. Database 23 Ref. Fluid Thermodyn. Transp. Prop. (REFPROP), Version 9.1*, 2013.

18   Mattei, Investment in Air Compressor Efficiency, https://web.archive.org/web/20100509233715/http://www.matteicomp.com/compressor-news.htm?id=165176063, (accessed 9 May 2010).

19   I. Renewable Energy Agency, *IRENA: Renewable Power Generation Costs in 2017*, 2018.

20   Mattei, Mattei Compressor Advantages, https://web.archive.org/web/20100417160607/http://www.matteicomp.com/compressor-operating-principles/, (accessed 17 April 2010).